Chinese Chemical Letters 32 (2021) 3584–3590

Contents lists available at ScienceDirect

Chinese Chemical Letters

journal homepage: www.elsevier.com/locate/cclet

Communication

Angle-independent responsive organogel retroreflective structural color film for colorimetric sensing of humidity and organic vapors

Cuiping Ji, Jing Zeng, Sijia Qin, Min Chen*, Limin Wu

Department of Materials Science and State Key Laboratory of Molecular Engineering of Polymers, Fudan University, Shanghai 200433, China

ARTICLE INFO

Article history:
Received 5 January 2021
Received in revised form 14 March 2021
Accepted 22 March 2021
Available online 24 March 2021

Keywords:
Angle-independent structural color
Colorimetric sensing
Responsive retroreflective structural color film
Humidity sensing
VOC vapor sensing

ABSTRACT

The angle dependence of photonic crystals (PCs) dramatically limits their practical applications in the colorimetrical sensing of humidity and volatile organic compound (VOC) vapors. In addition, it is challenging for inverse opal PCs to colorimetrically distinguish between vapors with similar refractive indices. Different from the mechanism of PC-based sensors, here, we report an angle-independent polyacrylamide (PAAm) organogel structural color film based on the mechanisms of retroreflection, total internal reflection (TIR) and interference with a shape similar to a single-sided "egg waffle". During the process of responding to humidity and VOC vapors, the color of the film remains angle-independent in the normal angle range of 0° to 45° under coaxial illumination and observation conditions. At the same time, the film can colorimetrically distinguish between vapors with similar refractive indices, such as methanol and ethanol, which is mainly due to the differences in their polarity and solubility parameters. The film shows good stability, reversibility and selectivity when exposed to vapors. A colorimetric sensor with a new response mechanism is proposed and has the potential to effectively distinguish between vapors with similar refractive indices. Furthermore, this responsive retroreflective structural color film (RRSCF) provides a universal strategy to develop targeted angle-independent structural color sensors by selecting optimized materials.

Humidity sensing is significant for industrial processing, human health, and storage of instruments, food, and artworks [1]. The detection of organic vapors, VOCs especially, is essential for daily life for applications ranging from air quality monitoring in the laboratories and homes to industrial safety [2]. Thus, various sensors, such as colored indicators for colorimetric sensing [3,4], F-containing receptor fluorescent polymer probes [5], single-nanoparticle-layer plasmonic film sensors [6], metal oxide semiconductor sensors [7,8] and covalently linked metal-organic framework-polymer resin sensors [9], have been developed. Among them, colorimetric sensing is a more direct and convenient detection method, because the results can even be perceived by the naked eyes.

Smart stimuli-responsive structural color materials have attracted tremendous attention for decades due to their promising applications in sensing [10–14], indicating [15,16], anti-counterfeiting [17–21], and patterning [22–26]. A variety of structural color materials, such as photonic crystals [27–33], *Morpho* butterflies [34–37] and their mimics [38], hydrogels [39–41], organogels [42], Bragg stacks [43–46], nanocrystals [47–50] and layer-by-layer (LBL) films [51], have been used for a long time to develop humidity and organic vapor sensors. Among them, opal and inverse opal PCs have been widely exploited for colorimetric sensing owing to their tunable photonic stopband. Tian *et al.* reported a humidity sensitive polyacrylamide-poly(styrene-methyl methacrylate-acrylic acid) (PAAm-P(St-MMA-AA)) PC hydrogel. The color was varied owing to the increase in its lattice spacing [41]. Diao *et al.* developed a silk-fibroin inverse opal PC as a humidity sensor. The cyclic contraction of silk fibroin induced by humidity accounted for the changing lattice constants [52]. In regard to VOC vapor sensing, inverse opal PCs are widely exploited owing to their abundant ordered voids. The effective refractive index (RI) of inverse opal PCs increases because vapors with a higher RI than air entirely or partially replace the air in the voids. Therefore, the photonic stopband shifts, and the color changes [3,53]. However, there remain two challenges in the practical applications of PC colorimetric sensors in the detection of humidity and organic vapors: (1) Achieving angle-independent colors is challenging. Due to the angle dependence of PCs, the sensors should be observed at the same angle (usually in the normal direction) to guarantee the reliability of the color change. Although amorphous photonic structures (APSs) [54,55], black additives [56,57] and artificial

* Corresponding author.
E-mail address: chenmin@fudan.edu.cn (M. Chen).

https://doi.org/10.1016/j.cclet.2021.03.058

melanin particles [58] or composites [59,60] are used to reduce the angle dependence and increase the saturation of the color, the systems become more complicated when they are applied in colorimetric sensing, and it is rarely investigated whether the angle independence can be maintained during the response. (2) Colorimetrically distinguishing between vapors with the same or similar RI by pure inverse opal PCs is also difficult. This is because the color change mechanism of pure inverse opal PC sensors is related to the changes in the effective RI.

Besides the Bragg diffraction of PCs, structural colors can also be ascribed to interference and retroreflection mechanisms. Recently, Goodling *et al.* reported a brilliant structural color within monodisperse biphasic Janus oil droplets, in which the color was generated due to total internal reflection (TIR) and interference of light at a concave optical interface [61]. Retroreflection, a special kind of reflection, is defined as that reflected light returns to the light source from the reverse direction of the incident light [62]. And retroreflective materials have been widely used in traffic signs [63,64]. Currently, retroreflective materials are mostly prepared by glass beads or corner cubes, and the undercoating layer containing pigments or dyes accounts for the coloration [62,63,65]. Recently, our group developed a retroreflective structural color film (RSCF) for smart displays based on retroreflection and thin-film interference. The RSCF showed a non-iridescent vivid structural color under coaxial illumination and observation conditions (*i.e.*, the direction of illumination is the same as that of observation) [66], which is advantageous for colorimetric sensors.

Herein, inspired by these exciting studies, we report an angle-independent responsive retroreflective structural color film (RRSCF) based on the mechanisms of retroreflection, TIR and interference, which are completely different from PCs. The RRSCF was made by the PAAm organogel, with a shape similar to a single-sided "egg waffle", that is, one side is a plane, and the other side is a *quasi*-hemisphere monolayer array. The fabricated RRSCF revealed its sensitivity to humidity, especially high humidity, according to the color changes and reflectance spectra obtained with varied humidity. Furthermore, the sensor was also capable of acting as a VOC vapor visual sensor according to the apparent changes in its colors and the reflectance spectra obtained during the methanol and ethanol vapor sensing experiments. Note that the RRSCF remains non-iridescent within a normal angle range from 0° to 45° under coaxial illumination and observation conditions when it is exposed to various humidity conditions and VOC vapors. This is mainly due to the uniform volume change of *quasi*-hemispheres during the swelling process of the film, so the *quasi*-hemisphere array structure can be well maintained. This RRSCF showed reversibility and selectivity as well. These results indicate that this angle-independent RRSCF is a promising practical candidate for colorimetric sensing of humidity and vapors, and for discriminating between vapors with the same or similar refractive indices.

The closely packed microsphere monolayer array was obtained by unidirectional rubbing 14 μm polymethyl methacrylate (PMMA) microspheres on a polydimethylsiloxane (PDMS) substrate [67,68]. Then, a transparent tape was used to transfer the array to the sticky layer of tape to fabricate the retroreflective structural color film (RSCF) [66]. Afterward, the RSCF was utilized as the first template to prepare the PDMS replica template. Briefly, PDMS prepolymers and curing agents (10:1, w/w) were mixed thoroughly and then poured onto the RSCF template. A PDMS template with a *quasi*-hemisphere array structure was easily obtained by peeling off the PDMS after curing at 40 °C for 72 h. Thereafter, the cavities of the PDMS template supported by the Petri dish were filled with acrylamide (AAm) pre-gel ethanol solution. The pre-gel solution contains 15 wt% AAm, 0.45 wt% *N*,*N*′-methylene diacrylamide as a crosslinking agent, and 0.45 wt% Irgacure 2959 as a photoinitiator. Photopolymerization was carried out by 310 nm UV irradiation for approximately 20 min. Finally, the RRSCF with a 14 μm-diameter *quasi*-hemisphere monolayer array structure (denoted as 14 μm-RRSCF) was obtained after drying for 72 h in an ambient atmosphere and removing the PDMS template. By adjusting the diameter of the microspheres used in the RSCF templates (including 4 μm, 5 μm, 6 μm, 7 μm, 8 μm, 10 μm, 13 μm, 15 μm and 20 μm), PDMS templates with cavities of different diameters were obtained. Consequently, RRSCFs with different diameters of *quasi*-hemisphere array structures were obtained *via* different PDMS templates.

Two pieces of RRSCFs were placed in a customized humidity chamber (Fig. S1a in Supporting information). To record the reflectance spectra, one was placed horizontally with its plane surface facing down. To capture the digital photographs, the other was stuck to the vertical sealing film with its plane surface forward. The RH was controlled by adjusting the mixing ratio of dry nitrogen and wet nitrogen in the chamber. The rate that the RH was changed was kept at approximately 0.33%–0.50% RH/min, which was monitored by a hygrometer with an accuracy of 3% RH (GSP-8, Jingchuang). Reflectance spectra were recorded from ambient RH (approximately 50% RH) to 99% RH, and photographs of the RRSCFs were captured simultaneously. Angle-resolution reflectance spectra were recorded when the film was exposed to various RH conditions. Experiments for the RRSCFs with other sizes were carried out with the same method.

A customized quartz chamber with an inlet and outlet (Fig. S1b in Supporting information) was used for vapor sensing measurements. The placement of the two 14 μm-RRSCFs in the chamber was similar to that in the RH sensing experiments. For the saturated methanol vapor sensing experiments, reflectance spectra were recorded as soon as the sample was put into the chamber with saturated methanol vapor. Afterward, air was aerated into the chamber to remove the vapors, and reflectance spectra were recorded simultaneously. For the reversibility experiments, reflectance spectra were recorded with the same method used for the saturated methanol vapor sensing experiment. For the general VOC vapor sensing experiments, 5 mL organic solvents were injected once into a container in the chamber *via* a syringe. Simultaneously, reflectance spectra were recorded at a specific time interval, and photographs were captured. Angle-resolution reflectance spectra were recorded when the film was exposed to vapors.

Scheme 1 schematically illustrates the fabrication procedures and sensing mechanism of the RRSCF. In brief, the PDMS template was peeled off from a 14 μm-RSCF template after curing. Afterward, the PDMS template was put into a Petri dish filled with acrylamide pre-gel solution. Finally, the RRSCF was obtained after UV polymerization. The RRSCF can be used as a colorimetric sensor for humidity and VOC vapors (methanol and ethanol). With exposure to humidity or vapors, the reflectance spectra and color alter due to the changes in the *quasi*-hemisphere volume, effective refractive index (RI), and RI contrast. These changes are ascribed to the diffusion and absorption of air with different contents of water

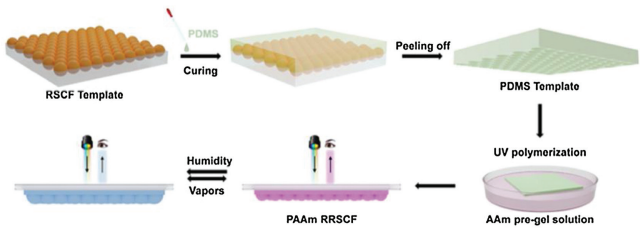

Scheme 1. Schematic illustration of the procedures used to fabricate the RRSCF and the sensing mechanism to humidity and vapors.

or VOC vapors into the film. Then, the film is swollen because PAAm molecules show a good affinity to water and VOC (methanol and ethanol). Details will be subsequently discussed.

From the top view and cross-sectional SEM images shown in Fig. S2a (Supporting information), it can be observed that the structure of the RSCF is a monolayer array of closely packed microspheres partially embedded into the sticky layer of the tape. The top-view and cross-section view SEM images of the PDMS template are displayed in Fig. S2b (Supporting information), which shows the bowl-shaped cavities with an ordered array. Correspondingly, the shape of the obtained RRSCF is similar to a single-sided "egg waffle", with a plane side and a *quasi*-hemisphere monolayer array side. SEM images are shown in Figs. 1a (top-view) and b (cross-section view). Digital photographs of RRSCF are shown in Fig. 1c, which depicts that RRSCF is purple-red when illuminated by a white light-emitting diode (LED) light source towards the plane side. Moreover, Figs. 1d-f show the digital photographs of the RRSCF with a white LED towards the array side and under diffuse daylight towards the array side and plane side, respectively. These photographs show the transparency of the film. The reflectance spectrum of RRSCF is shown in Fig. 1g, which agrees with the digital photographs. In addition, by adjusting the size of microspheres used in the RSCF templates, RRSCFs with different colors were obtained. Corresponding reflectance spectra and digital photographs are shown in Fig. S3 (Supporting information), indicating a universal method to prepare colored RRSCFs. When light propagates in the film along different trajectories, interference of the light that undergoes total internal reflection (TIR) at the interface between the *quasi*-hemispheres of RRSCF and outside air occurs, resulting in the generation of retroreflective structural color (Fig. 1h).

Fig. 1i shows the schematic diagram of the film tested at different angles under coaxial illumination and observation conditions. Figs. 1j and k show the angle-resolution reflectance spectra and corresponding digital photographs of the RRSCF illuminated from 0° to 45°. The results indicate that the RRSCF is non-iridescent under this condition, owing to the mechanisms of retroreflection, TIR, and interference. Thus, a consistent color can be observed in a wide range of angles, which is advantageous for a sensor. In addition, the path length of light propagating in the film increases as the angle of incidence increases, resulting in increased light absorption and scattering. As a result, the reflectivity gradually decreases.

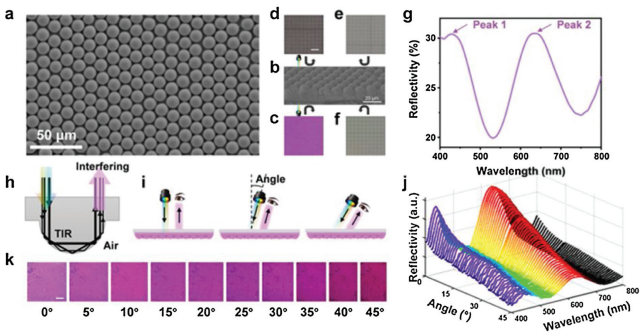

Fig. 1. (a) The top-view and (b) cross-section view SEM images of the RRSCF. The digital photographs captured under a white LED light source towards the (c) plane side and (d) array side and captured under diffuse daylight directed towards the (e) array side and (f) plane side. (g) Reflectance spectrum obtained with the probe normal to the plane side of the RRSCF. (h) Schematic diagram of generation of retroreflective structural color. (i) Schematic diagram, (j) angle-resolution reflectance spectra, and (k) digital photographs of the RRSCF under coaxial illumination and observation conditions within the angle range of 0° to 45°. Scale bar: 2 mm.

A series of humidity sensing experiments were carried out in a customized chamber (Fig. S1a) with a controllable relative humidity (RH), and details were described above. According to the reflectance spectra (Fig. 2a) and corresponding peak 1 and peak 2 positions (Fig. 2b), peak 1 and peak 2 are redshifted by only 4 nm and 14 nm as the RH was increased from 50% RH to 75% RH. The maximum redshifts for peak 1 and peak 2 are observed to be 79 nm and 71 nm as the RH was increased from 50% RH to 80% RH. In addition, visual sensing for humidity is realized owing to the color changes, from purple-red at 50% RH to yellow-red at 80% RH (Fig. 2c). Consequently, the RRSCF is more suitable for a particular condition, such as precise instrument storage where a high RH must be monitored. To investigate whether the film can remain non-iridescent when the humidity changes, angle-resolution reflectance spectra at 78% RH were recorded under coaxial illumination and observation conditions (Fig. 2d). There is no shift for the two peaks from 0° to 45°, indicating that our film is an angle-independent structural color sensor. This is mainly due to the uniform volume change of the *quasi*-hemispheres during the swelling of the film, so the *quasi*-hemisphere array structure can be well maintained. The angle-independent color of the RRSCF makes it possible to observe reliable and consistent results at any position within a large angle range of 0° to 45°, thereby greatly improving the practicality of the colorimetric humidity sensor.

Moreover, humidity sensing experiments were also carried out for 10 μm-, 13 μm-, 15 μm- and 20 μm-RRSCFs with the same method, and the results are displayed in Fig. S4 (Supporting information). The two peak positions of the 10 μm-RRSCF are redshifted by 31 nm and 45 nm. The two peak positions of the 13 μm-RRSCF are redshifted by 25 nm and 26 nm. The two main peak positions at 416 nm and 706 nm of the 15 μm-RRSCF are redshifted by 23 nm and 42 nm, respectively. The two main peak positions at 503 nm and 575 nm of the 20 μm-RRSCF are redshifted by 28 nm and 54 nm, respectively. These results indicate a universal method for constructing a humidity sensor made by a responsive retroreflective structural color film.

Generally, the humidity sensitivity of the RRSCF is influenced by two factors: (1) The color is generated owing to interference of the light that undergoes TIR at the interface between the *quasi*-hemispheres of RRSCF and outside air [61]. Thus, the occurrence of TIR and interference is crucial for color generation, which depends on the RI contrast between the film and air outside. The effective RI of the RRSCF (n_{eff}) is defined as:

$$n_{eff}=\sqrt{n_{air}^2 f_{air}+n_{PAAm}^2(1-f_{air})} \quad (1)$$

where n_{PAAm} and n_{air} are the RI of the PAAm (n = 1.452) and air (n = 1.0) inside the film; f_{air}, (1-f_{air}) are the volume fraction of air inside the film and PAAm. Consequently, n_{eff} mainly depends on f_{air} because the change in n_{air} is negligible as RH increases. (2) The swelling degree of the film owes to the affinity of PAAm towards water. Once the humidity increases, the outside air with a higher water vapor content exchanges with the inside air with the original water vapor content, resulting in PAAm swelling. Therefore, the phenomenon described here results from the synergistic effect of these factors, and details are discussed as follows.

When RH increases, the water vapor content in the air increases. Due to the good affinity of PAAm towards water, PAAm is swollen when the air diffuses into the film. The volume increase of the *quasi*-hemispheres results in the increase of f_{air} and redshift of the peak position. Meanwhile, n_{eff} decreases because of the increased f_{air}. Therefore, the RI contrast between the film and air outside decreases, which has a negative effect on the occurrence of TIR. As RH continues to increase, the exposed *quasi*-hemispheres dissolve and connect due to solvation. As a result, the surface area of the *quasi*-hemispheres exposed to outside air reduces. Thus, the

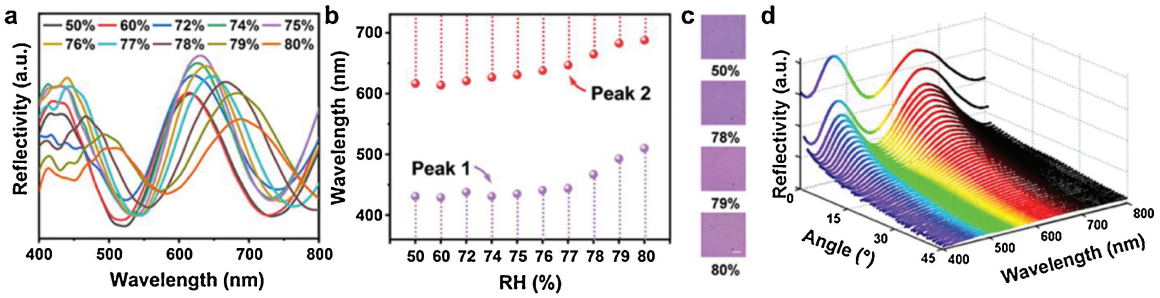

Fig. 2. (a) Reflectance spectra, (b) corresponding peak 1 and peak 2 positions and (c) digital photographs of the RRSCF exposed to different humidity conditions. (d) Angle-resolution reflectance spectra of the RRSCF at 78% RH. Scale bar: 2 mm.

amount of light that undergoes TIR continues to decrease until interference or TIR can no longer occur. Finally, the film becomes colorless. After the experiment, the monolayer array structure still remains, but the diameter of the original *quasi*-hemisphere increases for approximately 71% from 14 μm to 24 μm (Fig. S5 in Supporting information). This result validates the mechanism we proposed above. In addition, the *quasi*-hemisphere array structure fails to recover after RH decreases, which results in the failure of the reusability of the RRSCF. Therefore, the film is very suitable for humidity labels, showing that the humidity of the environment where the item is located has been as high as 80%. Thus, the item should be checked in time.

Due to its toxicity, methanol is very harmful to the human nervous system and blood system, so it is essential to detect methanol and its vapor. Moreover, methanol is one of the most commonly used VOCs in laboratories. The polarity of methanol is close to that of water. Therefore, methanol vapor is chosen to investigate the potential of the film for VOC vapor detection. Fig. 3 depicts the reflectance spectra of the RRSCF during the response process with exposure to saturated methanol vapor and during the recovery process with exposure to air. Two crests are stepwise redshifted and then blueshifted, which is attributed to changes in the volume of the swollen *quasi*-hemispheres, effective RI and RI contrast. For the response process, Fig. 3a shows the maximum redshifts of 28 nm and 40 nm for the two peaks. In addition, the appearance of a new peak is observed at 89 s. These results are mainly due to the increase in the size of *quasi*-hemispheres and the interference between the light that undergoes TIR. Afterward, the blueshift of 26 nm for peak 2 and the disappearance of peak 1 are observed at 122 s, which is mainly attributed to the decreased RI contrast. As soon as the film is exposed to air, it basically returns to the initial state within 24 s. Reflectance spectra are plotted in Fig. 3b. The rapid response process is due to the rapid diffusion and adsorption of methanol under a high vapor concentration, which causes the rapid change in RI and rapid expansion of the film.

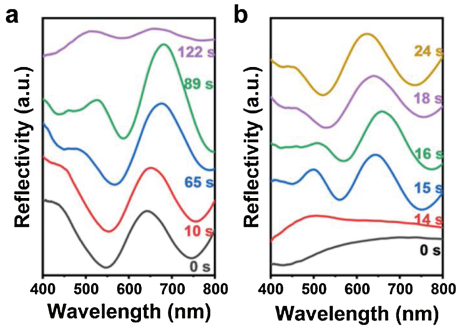

Fig. 3. Reflectance spectra of the RRSCF exposed to (a) saturated methanol vapor and (b) air.

When exposed to air, the RRSCF recovers quickly because methanol vapor escapes from the film quickly as the vapor concentration drops sharply. In addition, the response behaviors of 20 μm-RRSCF to saturated methanol vapor are similar to those of 14 μm-RRSCF. The maximum redshift of the main peak is 25 nm, and the maximum blueshift is 42 nm, as shown in Fig. S6 (Supporting information).

In general, the vapor sensing performance of the RRSCF is influenced by two factors: (1) The first is the RI contrast between the film and air outside. The effective RI of the RRSCF ($n_{RRSCF\text{-}eff}$) and air ($n_{air\text{-}eff}$) in the chamber are defined as:

$$n_{RRSCF-eff} = \sqrt{n^2_{air-eff} f_{air-eff} + n^2_{PAAm}(1-f_{air-eff})} \quad (2)$$

$$n_{air-eff} = \sqrt{n^2_{vap} f_{vap} + n^2_{air}(1-f_{vap})} \quad (3)$$

where n_{PAAm}, n_{air}, and n_{vap} are the RI of PAAm (n = 1.452), air except vapors (n = 1.0), and VOC vapors (listed in Table S1 in Supporting information); $f_{air\text{-}eff}$, (1 - $f_{air\text{-}eff}$), f_{vap}, and (1 - f_{vap}) are the volume fraction of air inside the film, PAAm, VOC vapors, and air except the VOC vapors inside the chamber, respectively. In this section, n_{vap} refers to the RI of methanol; f_{vap} refers to the volume fraction of methanol vapor. Consequently, $n_{RRSCF\text{-}eff}$ depends on $f_{air\text{-}eff}$ and $n_{air\text{-}eff}$; $n_{air\text{-}eff}$ depends on n_{vap} and f_{vap} (and equally to the vapor concentration). Note that the VOC vapors can influence $n_{air\text{-}eff}$ owing to the VOC vapors having a higher saturated vapor pressure than water. However, the change in $n_{air\text{-}eff}$ is slight. Thus, the change in $f_{air\text{-}eff}$ plays a dominant role in the change in $n_{RRSCF\text{-}eff}$. (2) The second factor affecting the vapor sensing performance of the RRSCF is the swelling degree of the film due to the affinity of PAAm towards VOC vapors and their differences in polarity and solubility parameters.

From the abovementioned, the phenomenon here is explained as follows: for the response process, due to saturation (*i.e.*, a high methanol vapor concentration), an increased f_{vap} results in a slight increase in $n_{air\text{-}eff}$. Along with the exchanges of air inside and outside the film, PAAm is swollen by methanol vapor, resulting in the volume increase of the *quasi*-hemispheres, redshift of the peak position, and increase in $f_{air\text{-}eff}$. At the same time, $n_{RRSCF\text{-}eff}$ decreases because the influence factor of $f_{air\text{-}eff}$ plays a dominant role, although $n_{RRSCF\text{-}eff}$ is also influenced by the slightly increased $n_{air\text{-}eff}$. Afterward, the RI contrast decreases owing to decreased $n_{RRSCF\text{-}eff}$ and increased $n_{air\text{-}eff}$, resulting in the blueshift of the peak position and decrease in the reflectivity. Finally, the film becomes colorless because interference or TIR can no longer occur. For the recovery process, $n_{air\text{-}eff}$ decreases quickly, owing to the sharply decreased methanol vapor concentration. Thus, the RI contrast increases, causing a redshift of the peak position at first. Afterward, the film shrinks owing to methanol vapor escaping out of the film, causing the peak position to blueshift to the initial peak position.

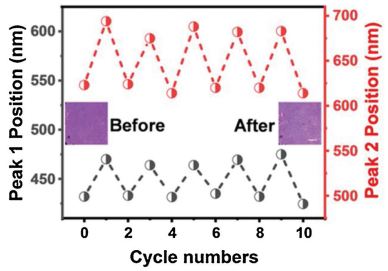

Fig. 4. Reversible peak position changes (the black curve for peak 1, the red curve for peak 2) for RRSCF with exposure to saturated methanol vapor and air alternately, and digital photographs (inset) of RRSCF before and after five cycles. Scale bar: 2 mm.

The RRSCF was tested alternately in the chamber with saturated methanol vapor and air for five cycles. The black and red curves in Fig. 4 depict the position changes for peak 1 and peak 2 throughout the response and recovery processes, respectively. The first trough is the original peak position, while the other troughs are the peak positions of the RRSCF at the end of every recovery process. The crests are the maximum redshift positions during every response process. As methanol vapor enters into and escapes out of the film, PAAm is swollen and de-swollen. Thus, the *quasi*-hemisphere structure changes (expands or shrinks). The RI contrast between the film and outside air also changes. Therefore, the peak position shifts accordingly. In addition, there is almost no change in the RRSCF before and after five cycles, according to the digital photographs (Fig. 4 inset). The results imply that our RRSCF sensor is well-stable and reusable.

Recently, due to the adverse impacts of ethanol on human consciousness, similar to methanol, the detection of ethanol has attracted widespread attention. However, it is challenging to colorimetrically distinguish between methanol and ethanol vapors by pure inverse opal PC sensor, owing to their similar refractive indices. Thus, methanol and ethanol vapors are chosen in this section to investigate the capacity of the RRSCF to distinguish between VOC vapors with similar refractive indices. Once methanol or ethanol is injected into the container inside the chamber, dynamic reflectance spectra (DRS) [42] of the RRSCFs are recorded continuously. Then, the DRS are converted to the contour maps shown in Fig. 5a for methanol vapor and Fig. 5b for ethanol vapor. The differences between the DRS patterns of methanol and ethanol vapors lie in the differences in their volatility, polarity, and solubility parameters. There is nearly no change at the early stage, because the vapor content is insufficient to swell PAAm. Afterward, owing to the better volatility of methanol, a shorter time is needed to reach a sufficient vapor content to swell the RRSCF. Thus, the pattern in Fig. 5a starts to change earlier than that in Fig. 5b. Fig. 5c shows the reflectance spectra and digital photographs of the RRSCF at the initial status and 5, 10, 15 and 20 min (corresponding to the white dotted line in Fig. 5a) after methanol injection. The color turns from purple-red to cyan-red as evaporation proceeds (in other words, the methanol vapor concentration increases), indicating that the RRSCF is a candidate for the visual sensing of methanol vapor. To intuitively illustrate the shift in the peak position, the crest positions of the spectra along with the evaporation time are plotted in Fig. 5d. Specifically, the maximum redshifts of the two peaks observed at 10 min are 17 nm and 26 nm. Then, the following maximum blueshifts of the two peaks are 34 nm at 17.5 min and 60 nm at 22.5 min. In addition, a new peak appears at 506 nm at 12.5 min. The explanation for this phenomenon has already been discussed in the previous section. Briefly, since PAAm is swollen by methanol vapor, the volume of *quasi*-hemispheres increases, resulting in the redshift of the peak position and the increase in $f_{air\text{-}eff}$. As evaporation proceeds, $n_{air\text{-}eff}$ increases continuously due to the increased vapor concentration. Simultaneously, $n_{RRSCF\text{-}eff}$ decreases mainly owing to the increased $f_{air\text{-}eff}$. Thus, the RI contrast between the RRSCF and air outside decreases, resulting in the blueshift of the peak position. A new peak appears due to the interference of the light that undergoes TIR at the interface of the *quasi*-hemispheres and air outside. Fig. 5e shows the angle-resolution reflectance spectra of the RRSCF within a normal angle range of 0° to 45° under coaxial illumination and observation conditions at approximately 17 min after methanol injection. The result shows that there is almost no change in the

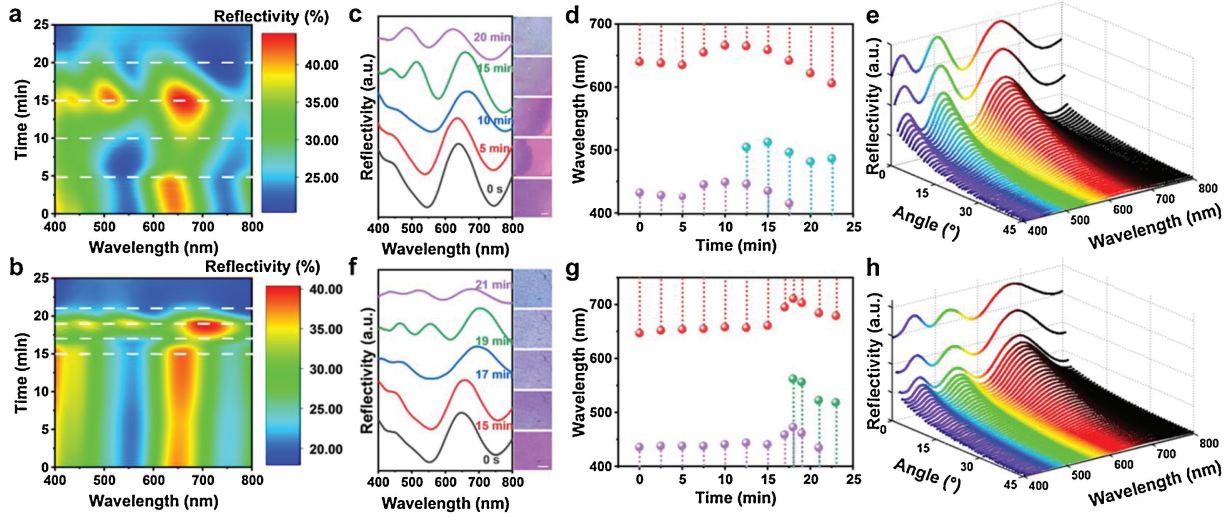

Fig. 5. The contour maps of the DRS of the RRSCF response to (a) methanol vapor and (b) ethanol vapor after injection. (c) Reflectance spectra and digital photographs at the initial status and 5, 10, 15 and 20 min after methanol injection, corresponding to the white dashed lines in (a); scale bar: 2 mm. (d) Peak positions at different exposure times to methanol vapor, purple spheres for peak 1, red spheres for peak 2, and cyan spheres for the new peak that appeared in the methanol vapor sensing experiment. (e) Angle-resolution reflectance spectra of the RRSCF under coaxial illumination and observation conditions, obtained at approximately 17 min after methanol injection. (f) Reflectance spectra and digital photographs at the initial status and 15, 17, 19 and 21 min after ethanol injection, corresponding to the white dashed lines in (b); scale bar: 1 mm. (g) Peak positions at different exposure times to ethanol vapor, purple spheres for peak 1, red spheres for peak 2, and green spheres for the new peak that appeared in the ethanol vapor sensing experiment. (h) Angle-resolution reflectance spectra of the RRSCF under coaxial illumination and observation conditions, obtained at approximately 20 min after ethanol injection.

peak position, proving that our sensor shows angle-independent color. Therefore, reliable and consistent results can be observed at any position in a large angle range, which greatly improves the practicability of the colorimetric sensor.

Similarly, Fig. 5f displays the reflectance spectra and digital photographs of the RRSCF at the initial status and 15, 17, 19 and 21 min (corresponding to the white dotted line in Fig. 5b) after ethanol injection. The color of the RRSCF changes from purple-red to a mixed color with a low saturation as the concentration of the ethanol vapor increases, indicating that the RRSCF is a candidate for the visual sensing of ethanol vapor. Fig. 5g shows the peak positions at different exposure times. The maximum redshifts of the two peaks observed at 18 min are 37 nm and 64 nm. Then, the following maximum blueshifts of the two peaks are 38 nm at 21 min and 32 nm at 23 min. In addition, a new peak appears at 562 nm. Fig. 5h shows the angle-resolution reflectance spectra of the RRSCF within a normal angle range of 0° to 45° under coaxial illumination and observation conditions at approximately 20 min after ethanol injection. The result shows that there is almost no change in the peak position, proving that our sensor is non-iridescent. In conclusion, the changes in the DRS and colors of the RRSCF are different in the two experiments. Principal components analysis (PCA) was carried out according to ref [34], and results are shown in Fig. S7 (Supporting information). It can be seen that the trajectories of methanol and ethanol vapors are different. Thus, our RRSCF can be a potential colorimetric sensor used to distinguish between methanol and ethanol vapors, even though they have similar refractive indices.

In addition, Fig. S8 (Supporting information) depicts the results of the methanol and ethanol vapor sensing experiments performed for 20 μm-RRSCF. Maximum redshifts of 39 nm, 21 nm, 14.5 nm and 68 nm are observed clearly for the four peaks 7.5 min after methanol injection. Maximum redshifts of 51 nm, 26 nm, 38 nm and 69 nm are observed clearly for the four peaks 17 min after ethanol injection. The changes in the DRS and colors of 20 μm-RRSCF are different in the two experiments, which indicates that our RRSCF sensor is an excellent candidate for colorimetrically distinguishing between methanol and ethanol vapors. Moreover, the phenomena of redshift first and then blueshift in the tests performed for 20 μm-RRSCF are the same as those performed for 14 μm-RRSCF, which validates the mechanism we proposed above.

The DRS of the RRSCF exposed to various VOCs were recorded to investigate the selectivity of the film towards methanol and ethanol vapors. Fig. 6a shows the 3D contour map of the DRS when the RRSCF was exposed to iso-propanol vapor. Then, the 3D contour map is converted to a 2D DRS pattern (Fig. 6b). DRS patterns of the RRSCF towards acetonitrile, dichloromethane, ethyl acetate, and toluene vapors are shown in Figs. 6c-f, respectively. Compared to methanol and ethanol vapors, the RRSCF shows a weaker affinity towards iso-propanol, acetonitrile, dichloromethane, ethyl acetate, and toluene vapors, owing to the mismatch of solubility parameters between the RRSCF and vapors. Thus, PAAm cannot be swollen, resulting in an unchanged $f_{air\text{-}eff}$. Although $n_{air\text{-}eff}$ increases slightly due to the increase in f_{vap}, $n_{RRSCF\text{-}eff}$ hardly changes. Therefore, there is nearly no shift in the peak positions in these DRS patterns. The results indicate the excellent detection selectivity of our sensor towards methanol and ethanol vapors.

In summary, this work presents an angle-independent responsive retroreflective structural color film (RRSCF) sensor based on the mechanisms of retroreflection, total internal reflection (TIR), and interference. A new response mechanism for the colorimetric sensing of humidity and VOC vapors is proposed; to summarize, the changes in the *quasi*-hemisphere volume which is due to the swollen PAAm, the changes in the effective refractive index (RI) and RI contrast. Redshifts of the peak position and changes in the color are observed when the humidity increases. In addition, the constructed RRSCF shows a fast response and recovery rate when alternatively exposed to saturated methanol vapor and air. Distinguishing between methanol, ethanol, and other VOC vapors with similar refractive indices is realized according to the changes in the DRS patterns and visible color observed by the naked eyes. Most importantly, when exposed to humidity, methanol and ethanol vapors, our RRSCF exhibits an angle-independent color within a normal angle range from 0° to 45° under coaxial illumination and observation conditions. Therefore, reliable and consistent results can be observed at any position in a large angle range, which greatly improves the practicability of the colorimetric sensor. In addition, this RRSCF supplies a universal strategy to

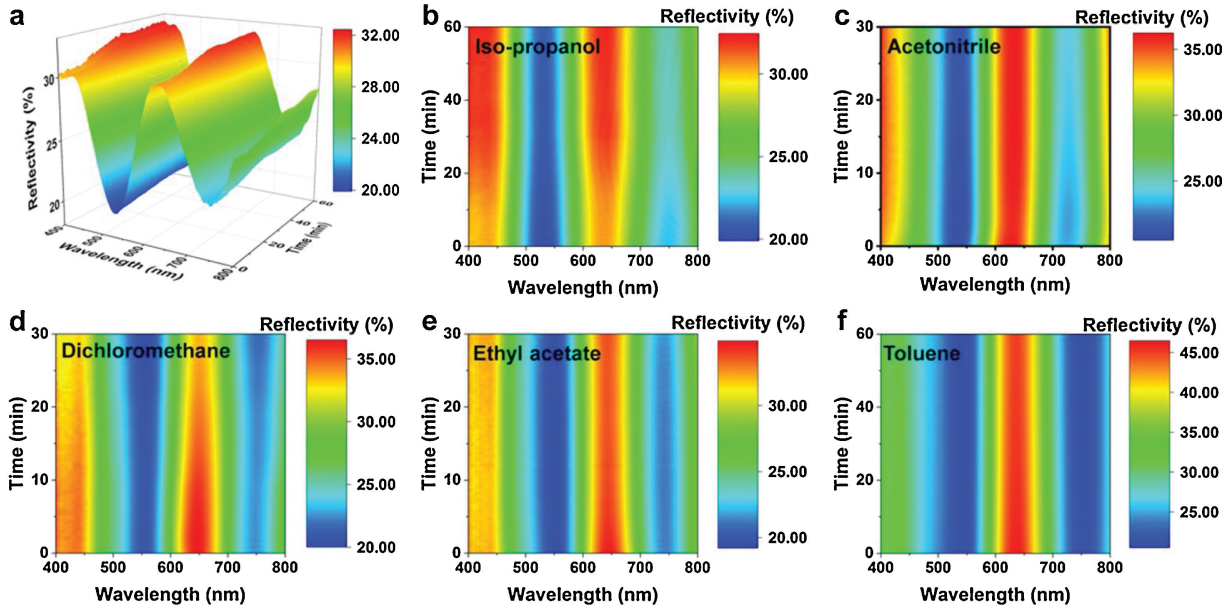

Fig. 6. (a) The 3D contour map of the DRS of the RRSCF response to iso-propanol vapor, with the wavelength at the x-axis, the time at the y-axis, and the reflectivity at the z-axis. The converted 2D DRS patterns of the RRSCF response to (b) iso-propanol vapor, (c) acetonitrile vapor, (d) dichloromethane vapor, (e) ethyl acetate vapor and (f) toluene vapor.

construct targeted sensors sensitive to corresponding stimuli (light, heat, electric and magnetic fields, *etc.*) by selecting proper materials. Thus, this RRSCF will broaden the investigation ranges of the responsive structural color domain. In the future, this RRSCF can also be promising in other applications, such as anti-counterfeiting and patterning.

Declaration of competing interest

The authors report no declarations of interest.

Acknowledgments

This work was supported by National Key Research and Development Program of China (Nos. 2017YFA0204600, 2018YFE0201701) and National Natural Science Foundation of China (No. 51673041).

Appendix A. Supplementary data

Supplementary material related to this article can be found, in the online version, at doi:https://doi.org/10.1016/j.cclet.2021.03.058.

References

[1] K. Lazarova, D. Christova, R. Georgiev, et al., Nanomaterials 9 (2019) 875.
[2] R. Potyrailo, R.R. Naik, Annu. Rev. Mater. Res. 43 (2013) 307–334.
[3] Y. Zhang, Y. Sun, J. Liu, et al., Sens. Actuator. B: Chem. 291 (2019) 67–73.
[4] Z. Dong, N. Zhang, Y. Wang, et al., Adv. Funct. Mater. 29 (2019) 1904453.
[5] Y. Yu, W. Xu, Y. Fu, et al., Dyes Pigm. 172 (2020) 107852.
[6] J. Shen, B. Luan, H. Pei, et al., Adv. Mater. 29 (2017) 1606796.
[7] P.K. Shihabudeen, A. Roy Chaudhuri, Sens. Actuator. B: Chem. 305 (2020) 127523.
[8] S. Nakata, N. Takahara, Sens. Actuator. B: Chem. 307 (2020) 127635.
[9] J. Ma, L.M. Zhao, C.Y. Jin, et al., Dyes Pigm. 173 (2020) 107883.
[10] Q. Xu, S.M. Mahpeykar, I.B. Burgess, et al., ACS Appl. Mater. Interfaces 10 (2018) 20120–20127.
[11] M. Xiao, Y. Li, J. Zhao, et al., Chem. Mater. 28 (2016) 5516–5521.
[12] Y. Hu, Y. Zhang, T. Chen, et al., ACS Appl. Mater. Interfaces 12 (2020) 45174–45183.
[13] D. Men, D. Liu, Y. Li, Sci. Bull. 61 (2016) 1358–1371.
[14] Y. Xia, S. Gao, H. He, et al., J. Phys. Chem. C 124 (2020) 16083–16089.
[15] F. Fu, L. Shang, Z. Chen, et al., Sci. Robot. 3 (2018) eaar8580.
[16] Y. Fang, Y. Ni, B. Choi, et al., Adv. Mater. 27 (2015) 3696–3704.
[17] C. Liu, Z. Fan, Y. Tan, et al., Adv. Mater. 32 (2020) 1907569.
[18] J. Chen, L. Xu, X. Lin, et al., J. Mater. Chem. C 6 (2018) 7767–7775.
[19] C.Y. Peng, C.W. Hsu, C.W. Li, et al., ACS Appl. Mater. Interfaces 10 (2018) 9858–9864.
[20] A.C. Arsenault, T.J. Clark, G. von Freymann, et al., Nat. Mater. 5 (2006) 179–184.
[21] K. Chen, Y. Zhang, J. Ge, ACS Appl. Mater. Interfaces 11 (2019) 45256–45264.
[22] M.M. Ito, A.H. Gibbons, D. Qin, et al., Nature 570 (2019) 363–367.
[23] F. Liu, S. Zhang, X. Jin, et al., ACS Appl. Mater. Interfaces 11 (2019) 39125–39131.
[24] K. Zhong, J. Li, L. Liu, et al., Adv. Mater. 30 (2018) 1707246.
[25] X. Du, J. Wang, H. Cui, et al., ACS Appl. Mater. Interfaces 9 (2017) 38117–38124.
[26] Y. Yue, T. Kurokawa, ACS Appl. Mater. Interfaces 11 (2019) 10841–10847.
[27] J. Xie, M. Duan, P. Bai, et al., Anal. Chem. 91 (2019) 1133–1139.
[28] C. Xiong, M. Pan, L. Wang, et al., Chem. Asian J. 13 (2018) 3670–3675.
[29] L. Wang, J. Wang, Y. Huang, et al., J. Mater. Chem. 22 (2012) 21405–21411.
[30] R. Xuan, Q. Wu, Y. Yin, et al., J. Mater. Chem. 21 (2011) 3672–3676.
[31] Y. Yu, S. Brandt, N.J. Nicolas, et al., ACS Appl. Mater. Interfaces 12 (2020) 1924–1929.
[32] H. Yang, L. Pan, Y. Han, et al., Appl. Surf. Sci. 423 (2017) 421–425.
[33] W. Zhang, M. Xue, K.J. Shea, et al., Chin. Chem. Lett. 32 (2020) 587–590.
[34] R.A. Potyrailo, H. Ghiradella, A. Vertiatchikh, et al., Nat. Photonics 1 (2007) 123–128.
[35] R.A. Potyrailo, T.A. Starkey, P. Vukusic, et al., Proc. Natl. Acad. Sci. U.S.A. 110 (2013) 15567–15572.
[36] J. Kittle, B. Fisher, C. Kunselman, et al., Sensors 20 (2020) 157.
[37] J.D. Kittle, B.P. Fisher, A.J. Esparza, et al., ACS Omega 2 (2017) 8301–8307.
[38] R.A. Potyrailo, R.K. Bonam, J.G. Hartley, et al., Nat. Commun. 6 (2015) 7959.
[39] M. Qin, M. Sun, R. Bai, et al., Adv. Mater. 30 (2018) 1800468.
[40] J.E. Stumpel, E.R. Gil, A.B. Spoelstra, et al., Adv. Funct. Mater. 25 (2015) 3314–3320.
[41] E. Tian, J. Wang, Y. Zheng, et al., J. Mater. Chem. 18 (2008) 1116–1122.
[42] Y. Zhang, Q. Fu, J. Ge, Nat. Commun. 6 (2015) 7510.
[43] P. Lova, G. Manfredi, L. Boarino, et al., ACS Photonics 2 (2015) 537–543.
[44] D. Kou, W. Ma, S. Zhang, et al., ACS Appl. Mater. Interfaces 10 (2018) 41645–41654.
[45] P. Lova, C. Bastianini, P. Giusto, et al., ACS Appl. Mater. Interfaces 8 (2016) 31941–31950.
[46] W. Ma, S. Li, D. Kou, et al., Dyes Pigm. 160 (2019) 740–746.
[47] S. Kano, K. Kim, M. Fujii, ACS Sens. 2 (2017) 828–833.
[48] G. Zhao, Y. Zhang, S. Zhai, et al., ACS Appl. Mater. Interfaces 12 (2020) 17833–17844.
[49] S. Pan, M. Chen, L. Wu, ACS Appl. Mater. Interfaces 12 (2020) 5157–5165.
[50] K. Yao, Q. Meng, V. Bulone, et al., Adv. Mater. 29 (2017) 1701323.
[51] D. Kou, Y. Zhang, S. Zhang, et al., Chem. Eng. J. 375 (2019) 121987.
[52] Y.Y. Diao, X.Y. Liu, G.W. Toh, et al., Adv. Funct. Mater. 23 (2013) 5373–5380.
[53] J. Liu, Y. Zhang, R. Zhou, et al., J. Mater. Chem. C 5 (2017) 6071–6078.
[54] L. Bai, V.C. Mai, Y. Lim, et al., Adv. Mater. 30 (2018) 1705667.
[55] Y. Takeoka, J. Mater. Chem. 22 (2012) 23299–23309.
[56] Y. Zhang, P. Han, H. Zhou, et al., Adv. Funct. Mater. 28 (2018) 802585.
[57] Q. Li, Y. Zhang, L. Shi, et al., ACS Nano 12 (2018) 3095–3102.
[58] M. Kohri, Y. Nannichi, T. Taniguchi, et al., J. Mater. Chem. C 3 (2015) 720–724.
[59] Y. Liu, C. Shao, Y. Wang, et al., Matter 1 (2019) 1581–1591.
[60] M. Xiao, Z. Hu, A.D. Tormo, et al., Sci. Adv. 3 (2017) e1701151.
[61] A.E. Goodling, S. Nagelberg, B. Kaehr, et al., Nature 566 (2019) 523–527.
[62] H. Kim, B. Lee, Opt. Eng. 46 (2007) 094002.
[63] T. Grosges, Opt. Mater. 30 (2008) 1549–1554.
[64] Y. Qi, C. Zhou, W. Niu, et al., Adv. Optical Mater. 8 (2020) 2001367.
[65] R.B. Nilsen, X.J. Lu, Retroreflection technology, in: T.P. Donaldson, C. Lewis (Eds.), Optics and Photonics for Counterterrorism and Crime Fighting, SPIE, London, 2004, pp. 47–60.
[66] W. Fan, J. Zeng, Q. Gan, et al., Sci. Adv. 5 (2019) eaaw8755.
[67] C. Park, T. Lee, Y. Xia, et al., Adv. Mater. 26 (2014) 4633–4638.
[68] Y. Wu, J. Zeng, Y. Si, et al., ACS Nano 12 (2018) 10338–10346.